JATIS Journal of Astronomical Telescopes, Instruments, and Systems

RESEARCH PAPER

New hope for obscured AGN: the PRIMA-NewAthena alliance

Luigi Barchiesi,[a,b,c,*] Francisco J. Carrera,[d] Cristian Vignali,[e,f] Francesca Pozzi,[e,f] Lucia Marchetti,[a,b,c] Carlotta Gruppioni,[f] Ivan Delvecchio,[f] Laura Bisigello,[g] Francesco Calura,[f] James Aird,[h] and Mattia Vaccari[a,b,c,i]

[a]University of Cape Town, Department of Astronomy, Cape Town, South Africa
[b]University of Cape Town, Inter-University Institute for Data Intensive Astronomy, Department of Astronomy, Cape Town, South Africa
[c]INAF-Istituto di Radioastronomia, Bologna, Italy
[d]IFCA (CSIC-University of Cantabria), Santander, Spain
[e]Università di Bologna, Dipartimento di Fisica e Astronomia (DIFA) "Augusto Righi", Bologna, Italy
[f]Istituto Nazionale di Astrofisica (INAF) - Osservatorio di Astrofisica e Scienza dello Spazio (OAS), Bologna, Italy
[g]Istituto Nazionale di Astrofisica (INAF) - Osservatorio Astronomico di Padova, Padova, Italy
[h]University of Edinburgh, Institute for Astronomy, Royal Observatory, Edinburgh, United Kingdom
[i]University of the Western Cape, Inter-University Institute for Data Intensive Astronomy, Department of Physics and Astronomy, Cape Town, South Africa

ABSTRACT. Understanding the AGN-galaxy co-evolution, feedback processes, and the evolution of Black Hole Accretion rate Density (BHAD) requires accurately estimating the contribution of obscured Active Galactic Nuclei (AGN). However, detecting these sources is challenging due to significant extinction at the wavelengths typically used to trace their emission. We evaluate the capabilities of the proposed far-infrared observatory *PRIMA* and its synergies with the X-ray observatory *NewAthena* in detecting AGN and in measuring the BHAD. Starting from X-ray background synthesis models, we simulate the performance of *NewAthena* and of *PRIMA* in Deep and Wide surveys. Our results show that the combination of these facilities is a powerful tool for selecting and characterizing all types of AGN. Although *NewAthena* is particularly effective at detecting the most luminous, the unobscured, and the moderately obscured AGN, *PRIMA* excels at identifying heavily obscured sources, including Compton-thick AGN (of which we expect 7500 detections per deg^2). We find that *PRIMA* will detect ~60 times more sources than *Herschel* over the same area and will allow us to accurately measure the BHAD evolution up to $z \sim 8$, better than any current IR or X-ray survey, finally revealing the true contribution of Compton-thick AGN to the BHAD evolution.

Keywords: infrared space observatory; infrared imaging; X-rays; hyperspectral imaging

Paper 24207SS received Dec. 3, 2024; revised Feb. 14, 2025; accepted Mar. 21, 2025; published Apr. 14, 2025.

1 Introduction

In the mid-1990s, the discovery of a tight correlation between the mass of supermassive black holes (SMBHs) and the stellar mass of the host galaxies[1–5] revealed a mutual influence between SMBHs and their host galaxies during their evolution. Notably, the relation between SMBH mass

*Address all correspondence to Luigi Barchiesi, luigi.barchiesi@uct.ac.za

and stellar mass, as well as with bulge mass, and gas and stellar velocity dispersions suggests a link between SMBH growth and star formation (SF), leading to the formulation of the AGN-galaxy co-evolution paradigm.[6–8] In this scenario, an intense phase of SF is triggered by wet mergers, particularly in the most luminous and massive systems,[9–12] or by *in situ* processes, such as rapid gas inflow and cooling of gas clumps.[8] A fraction of the galaxy's gas reservoir is funneled toward the SMBH, triggering active galactic nucleus (AGN) activity. Thus, this phase is marked by the concurrent growth of the SMBH and the galaxy stellar mass. Due to the large amounts of gas, most of the AGN radiation is absorbed through photoelectric absorption, causing the source to appear as an obscured AGN (with column density $N_{\rm H} \geq 10^{22}$ cm^{-2}). This phase is likely associated with the growth of obscured AGN in strongly star-forming submillimeter galaxies.[13–15]

However, we are far from having a complete picture of the galaxy co-evolution, and several key questions remain open: What mechanisms drive the co-evolution? What are the timescales involved? Is the co-evolution externally triggered (e.g., by galaxy mergers) or intrinsic to the galaxy evolution? To answer these questions, we need a comprehensive selection and study of obscured AGN across cosmic times.

The connection between the host galaxy and the SMBH is also evident in the similar evolutions of the BH Accretion rate Density (BHAD) and the Star Formation Rate Density (SFRD). Both peak at the "cosmic noon" ($z \sim 1-2$) and are characterized by significant uncertainties at redshifts $z > 3$,[16–18] primarily due to the challenges in detecting and accurately quantifying the contribution of obscured (i.e., dust-rich) sources at high redshifts. Furthermore, while the co-evolution up to the "cosmic noon" is widely accepted, there is no consensus yet on the fact that the SFRD and the BHAD still show similar evolution at higher redshift. In particular, although some works find a $z > 3$ decline of the BHAD similar to the one of the SFRD,[18–21] others argue for a flatter evolution.[22] Recently, the uncertainty on the high-z evolution of the BHAD has been exacerbated by the JWST discovery of "Little Red Dots" (LRDs), which if we assume to be dust-reddened broad-line AGN, provide BHAD measures more than one magnitude higher than the previous ones.[23]

A major challenge in addressing these questions is that most SMBH and host galaxy mass growth is expected to occur under heavily obscured conditions, making identifying and studying sources in this phase a daunting task.[24–26] In fact, the large quantity of gas and dust fueling both processes absorb the energy emitted by stars (at optical and UV wavelengths) and accreting SMBHs (in the X-ray, UV, and optical regimes), re-emitting it at longer wavelengths, primarily in the infrared (IR, $\sim 1-1000$ μm). One solution is to study the primary emission indirectly, by measuring dust-reprocessed radiation in the IR. The efficacy of identifying obscured AGN by selecting bright mid-IR sources with faint optical or near-IR emission has been demonstrated by *Spitzer*[27–29] and *WISE*.[30,31] Observations in this wavelength range provide insights into the physical processes occurring in obscured regions, allowing estimates of SFRD and BHAD, provided the two contributions can be properly disentangled. Space-based IR observatories enable direct measurement of dust-obscured SF activity, without requiring correction for dust attenuation. Mid- to far-IR photometric observations in deep fields[32,33] have produced estimates of SFRD and BHAD up to redshifts of $z \sim 3$,[32,34,35] using *Herschel PACS* data (100 and 160 μm).[36] However, the deepest cosmological surveys performed by *Herschel* at high redshifts have primarily detected the most luminous galaxies ($L_{\rm IR} > 10^{12}$ L$\odot$ at $z \geq 3$),[34] and they face challenges in accurately separating AGN and SF contributions, as the *Herschel* mission did not sample the mid-IR part where the AGN emission dominates.[37] Even when spectral energy distribution (SED) fitting is used to distinguish between these components, the assumption made in modeling them provides an additional source of uncertainties. Consequently, the initial phase of BH-galaxy co-evolution remains elusive and difficult to track.

One of the most effective methods for selecting unobscured or mildly obscured AGN is through X-ray observations, as the radiation from the innermost regions of the AGN can be directly detected.[38] However, the effectiveness of this approach diminishes with increasing column density (at $N_{\rm H} \geq 10^{24}$ cm^{-2}, the soft X-ray continuum is significantly attenuated). Even in deep field surveys, only a fraction of the most obscured AGN has been uncovered in the X-ray band.[39–42]

To summarize, the X-ray band is a powerful tool to select and characterize unobscured AGN, but it fails when heavily obscured sources are involved. On the other hand, the IR band does not suffer from source obscuration, but it has been limited to lower redshift than the X-rays and it relies on being able to properly disentangle the AGN and host-galaxy components.

Because the decommissioning of the *Spitzer* and *Herschel* space telescopes, the mid- and far-IR regimes have lacked instruments capable of detecting the emission from obscured galaxies and AGN beyond the local universe (while *WISE* is still operational, it has a wavelength coverage similar to JWST, i.e., it is not able to trace the mid- and far-IR at high-z).

In this paper, we introduce the key role of the PRobe far-Infrared Mission for Astrophysics (*PRIMA*; PI: J. Glenn) on[43–45] characterizing the population of obscured AGN and revealing the evolution of the BHAD at high redshift. *PRIMA* is a cryogenically cooled FIR observatory with a 1.8-m diameter, currently in the mission concept phase, with potential approval by 2026 and launch in 2032. Although the selection and characterization of AGN and galaxies with *PRIMA* have already been investigated in several works[46,47] (we refer to the *PRIMA* GO science book for an extensive list of *PRIMA* scientific cases),[45] here, we explore the synergies between *PRIMA* and the upcoming ESA X-ray observatory New Advanced Telescope for High ENergy Astrophysics (*NewAthena*), expected to be launched in the late 2030s, in detecting and characterizing obscured AGN at redshifts never reached before.

In Sec. 2, we give a brief description of the *PRIMA* and *NewAthena* instruments and surveys. The simulations of the intrinsic AGN predictions and our methods to estimate the detection capabilities of *NewAthena* and *PRIMA* are reported in Sec. 3. Section 3.2 explains how we simulated *PRIMA* measurements of the BHAD. The results are shown in Sec. 4, with the discussion of the capabilities of both instruments and their synergies in Sec. 5. In Sec. 6, we present our conclusions.

Throughout this paper, we adopt the following cosmological parameters: $H_0 = 70\ \mathrm{km\,s^{-1}\,Mpc^{-1}}$, $\Omega_M = 0.3$, and $\Omega_\Lambda = 0.7$.[48]

2 Instruments and Surveys

2.1 PRIMA

PRIMA is a proposed far-infrared (FIR) observatory equipped with a cryogenically cooled 1.8-m diameter telescope, specifically engineered for ultra-high sensitivity imaging and spectroscopic studies in the $24-235\ \mu$m wavelength range. Its design is optimized for the efficient survey of large areas, making it a powerful tool for wide-field astrophysical observations. The current *PRIMA* design incorporates two scientific instruments: *FIRESS* and *PRIMAger*. *FIRESS* is a versatile, multi-mode survey spectrometer covering wavelengths between 24 and 235 μm, offering both low-resolution ($R \sim 100$) and high-resolution ($R \sim 4400-12000$) in Fourier transform spectrometer mode. *PRIMAger*, on the other hand, will have two cameras able to operate at the same time: the PRIMA Hyperspectral Imager (PHI)—providing hyperspectral linear variable filters across two bands at $R = 10$ (PHI1 and PHI2) from 24 to 80 μm,—and the PRIMA Polarimetric Imager (PPI), which will use four filters to cover the $80-261\ \mu$m range with imaging and polarimetric capabilities. Thanks to its cryogenic cooling and advanced kinetic inductance detectors,[49–51] *PRIMA* will provide a mapping speed up to four orders of magnitude higher than *Herschel* at 100 μm and at $\sim$2 dex better than *Spitzer* at 24 μm.[45] Moreover, it has been shown that the contiguous coverage from 24 μm to 261 μm (paired with deblending techniques and possibly shorter wavelength priors) will allow us to reliably measure source fluxes up to one order of magnitude below the classical confusion limit[52] (the classical confusion limit being defined as 5 times the confusion noise, the latter obtained from 5σ-clipping the simulated maps until the convergence of the standard deviation[46]).

In this work, we will focus only on the *PRIMAger* instrument, as it is the best suited to perform large-area surveys. To simulate the *PRIMAger* Hyperspectral Imager, we approximated it as a series of 12 narrow filters, with center wavelengths and widths closely resembling the $R = 10$ capabilities of *PRIMAger* PHI. For the PRIMA Polarimetric Imager, we focused only on its total intensity sensitivity.

As *PRIMA* is still in the design phase and an official survey strategy has not been developed yet, we will use two example surveys. A Deep survey covering 1 deg^2 for a total of 1000 h (overhead included) and a Wide survey of 1000 h covering 28 deg^2. Table 1 summarizes the

Table 1 Reference surveys used in this work. t_{field} refers to the on-source time per pointings excluding overheads, t_{tot} to the survey total time including overheads. Due to its instrument design, *PRIMAger* is not able to perform snapshots; instead, it relies on panning along one direction when scanning its field. The deepest layer of *NewAthena* surveys comprises 30,300 ks fields for a total of 12 deg^2 and 2500 h (excluding overhead); however, for our Deep survey, we focused only on 1 deg^2 of it to be able to perform a comparison with the *PRIMA* deepest layer. The sensitivities of *PRIMA* are reported for the most and least sensitive bands (i.e., ∼25 μm and ∼235 μm, respectively) for a 5σ detection and have been calculated from the latest *PRIMAger* characteristics available in https://prima.ipac.caltech.edu/page/instruments. For the Deep survey, the first seven filters are always above the classical confusion limits, and it has been demonstrated that using those as priors, the flux in the confused bands can be recovered with a ∼20% accuracy.[52] For *NewAthena*, we report the 2 to 10 keV 5σ sensitivities.

Survey	Area	Instrument	t_{field} (ks)	t_{tot} (h)	Sensitivity
Deep	1 deg^2	*PRIMAger*		1000	92 – 229 μJy
		NewAthena WFI	300	>200	$1 - 2 \times 10^{-16}$ erg s^{-1}
Wide	28 deg^2	*PRIMAger*		1000	486 – 1211 μJy
		NewAthena WFI	200	∼4000	$1.5 - 3 \times 10^{-16}$ erg s^{-1}

survey strategy used in this work. In terms of confusion effects, our current survey strategy reaches sensitivity below the confusion limit starting from the 8th filter (PHI2 at ∼50 μm).[52] However, it has been demonstrated that even with a 1500 h survey, catalogs with a 95% purity can be produced for the first six filters (i.e., covering the lowest wavelength intervals). Using these as priors, the flux in all the confused bands can be recovered with an accuracy of 20%.[52]

2.2 New Athena

NewAthena is the upcoming ESA flagship X-ray observatory, designed to operate in the 0.2–12 keV energy range and address the "Hot and Energetic Universe" scientific theme.[53] The mission has recently completed a redefinition process to meet ESA's cost constraints, with the launch planned for the end of the 2030s. *NewAthena* features three key components in its scientific payload: an X-ray telescope with a 12-m focal length, along with two instruments. These include the X-ray Integral Field Unit (X-IFU),[54] which will provide high-spectral-resolution imaging, and the Wide Field Imager (WFI),[55] designed for moderate-resolution spectroscopy over a large field of view (FoV). The X-IFU on *NewAthena* will deliver simultaneous spatially resolved high-resolution X-ray spectroscopy, with a pixel size of 5 arcseconds and full-width at half maximum (FWHM) energy resolution of less than 4 eV below 7 keV, over a limited FoV of ∼4 arcminutes in diameter. By contrast, the WFI will offer sensitive wide-field imaging and spectroscopy, with an energy resolution of FWHM $\leq$ 170 eV at 7 keV, over a broader FoV and a wide energy range from 0.2 to 15 keV. The WFI achieves this using two sets of silicon-based DEPFET Active Pixel Sensor detectors: the large detector array, a 2×2 mosaic covering a $\sim 40 \times 40$ arcmin^2 FoV, oversampling the point spread function (PSF) by more than a factor of two, and the fast detector, optimized for high count-rate observations.

In this paper, we focus on the *NewAthena* WFI, as it is specifically designed for large-area surveys. Its capabilities are expected to efficiently complement those of *PRIMA*, enabling a comprehensive study of obscured and Compton Thick (CT, those with $N_H \geq 10^{24}$ cm^{-2})-AGN across multiple wavelengths.

The latest survey strategy envisioned for *NewAthena* is a "wedding cake" with three layers: a 12 deg^2 area covered by 30×300 ks pointings, a 28 deg^2 area covered by 70×200 ks pointings, and a 344 deg^2 area covered by 860×10 ks pointings (private communication). To properly study the synergies between *NewAthena* and *PRIMA*, we will compare the Deep 1 deg^2 *PRIMA* survey with 1 deg^2 of the *NewAthena* survey covered by 300 ks pointings (thus the maximum depth that *NewAthena* will deliver), and the 28 deg^2 *PRIMA* Wide survey with the 70×200 ks layer of the *NewAthena* survey (covering the same area). Table 1 summarizes the survey strategy used in this work.

3 Methods

3.1 NewAthena and PRIMA Detections

To assess the capabilities of *NewAthena* and *PRIMA* in detecting AGN, we adopted the approach of Barchiesi et al. (2021, hereafter B21),[56] modifying it to reflect the specifications of these new facilities. A detailed explanation of the method can be found in their work.

In summary, we began with the X-ray background (XRB) synthesis model of Gilli et al. (2007)[57] to estimate the total number of AGN as a function of redshift $z \in [0.3, 10]$, intrinsic 2–10 keV luminosity $\log(L_X/\mathrm{erg\,s^{-1}}) \in [42, 48.2]$, and hydrogen column density $\log(N_H/\mathrm{cm^{-2}}) \in [20,26]$. By incorporating the observational capabilities of *NewAthena*, we determined the fraction of the XRB that could be resolved while the unresolved fraction contributed to the background signal alongside the instrumental noise. A source was considered detected if it met a signal-to-noise ratio threshold of SNR >5, in which the SNR is defined as the total number of counts divided by the background counts.

For each bin, we assigned 20 SEDs drawn from a sample of 422 AGN in the COSMOS field with X-ray counterparts, high AGN significance, and similar L_X and N_H. The flux for each *PRIMAger* band was computed assuming a square transmission function. A source was considered to contribute to the detection fraction of its bin if its flux exceeded five times the sensitivity of the survey.

This process was repeated 42 times, selecting different SEDs in each iteration to ensure statistically robust estimates of the number of detected sources. The final detection estimates were taken as the median of these iterations, with uncertainties defined by the 16^{th}-84^{th} percentile range. Using 20 SEDs per bin, rather than one SED per expected detection, allowed us to optimize computational efficiency while minimizing the impact of stochastic SED selection, particularly in bins with a low number of expected sources.

In our simulations, we assumed that each detected source would also be recognized as an AGN. Although characterizing a source may be easy for the most luminous AGN or for those with X-ray coverage, it can be challenging for low-luminosity and very obscured AGN lacking *NewAthena* detections. We discussed this problem and how we can use *PRIMA* and a multi-wavelength approach to recognize AGN in Sec. 5.

3.2 Black Hole Accretion Rate Density

To investigate the capabilities of *PRIMA* in constraining the BHAD evolution, we required the AGN bolometric luminosity function (LF) as it would be derived from *PRIMA* observations. We used the same N_H binning as in Sec. 3.1; for the redshift, we chose 11 z bins, using the same binning as in Delvecchio et al. (2014, hereafter D14)[32] up to $z = 3.8$ and extending it up to $z = 10$. For the L_X binning, we started from 21 L_{bolo} bins in the range $9.5 \leq \log(L_{\mathrm{bolo}}/\mathrm{L_\odot}) \leq 19.5$ and converted those into L_X bins via the Lusso et al. (2012, hereafter L12) bolometric correction.[58] We simulated a *PRIMA* deep observation by extracting N SEDs in L_X, N_H, and z bins, where N is the expected number of objects (see Sec. 3.1). For each filter, we removed the sources with flux lower than the survey sensitivity and used the remaining ones to calculate the LF via the non-parametric $1/V_{\mathrm{max}}$ method,[59] where V_{max} denotes the maximum comoving volume within which each source is detectable. For each object, we determined the maximum redshift, z_{lim}, at which detection is possible within the survey's flux limits and computed the V_{max} as follows:

$$V_{\mathrm{max}} = \int_{z_{\mathrm{min}}}^{z_{\mathrm{max}}} \frac{dV}{dz} \Omega(z) \mathrm{d}z \tag{1}$$

where z_{min} is the lower boundary of each z bin and z_{max} is the minimum between the upper boundary and z_{lim}. $\Omega(z)$ is the projected area of the survey corrected for completeness (computed as $1/f_c$, with f_c the fraction of detected sources computed in Sec. 3.1).

For each L_{bolo} and z bin, we computed the LF as follows:

$$\Phi(L_{\mathrm{bolo}}, z) = \frac{1}{\Delta \log L_{\mathrm{bolo}}} \sum_{i=1}^{n} \frac{1}{V_{\mathrm{max},i}} \tag{2}$$

with $\Delta \log L_{\mathrm{bolo}}$ being the width of the L_{bolo} bin. With a nonlinear least square fitting algorithm, we fit the LFs with modified Schechter functions:[60]

$$\Phi(L)\mathrm{d}\ \log\ L = \Phi^*\left(\frac{L}{L^*}\right)^{(1-\alpha)} \exp\left[-\frac{1}{2\sigma^2}\log_{10}^2\left(1+\frac{L}{L^*}\right)\right]\mathrm{d}\ \log\ L \tag{3}$$

where L^* and Φ^* are the luminosity and the normalization of the knee of the LF, while σ and α are the slopes of the LF below and above the knee. The modified Schechter function has four free parameters, as we have between 3 and 7 (depending on the z) bins to fit it; thus, with 0 to 3 degrees of freedom, we decided to fix the slopes to the best-fit values found by D14, i.e., $\alpha = 1.48$ and $\sigma = 0.54$.

Finally, the BHAD evolution is obtained from

$$\Psi_{\mathrm{BHAD}}(z) = \int_0^\infty \frac{1-\epsilon}{\epsilon c^2} L_{\mathrm{bolo}}\Phi(L_{\mathrm{bolo}})d\ \log\ L_{\mathrm{bolo}} \tag{4}$$

with ϵ being the radiative efficiency of the SMBH, assumed to be $\epsilon = 0.1$.[61,62] While $\epsilon = 0.1$ it is the standard common assumption (e.g., Refs. 23, 61, and 62), we note that there is no general consensus on its value, with several works measuring ϵ as high as $\sim$0.4,[63–65] while BH modeling predicts values between 0.06 (for Schwartzschild BH) and 0.42 (for a maximally rotating BH). For this work, assuming higher values would simply lower the normalization of the BHAD, without changing its shape. Similarly to D14, we computed the uncertainties by performing the SED extraction and LF fitting 100 times.

4 Results

In this section, we illustrate the results of our simulations. As an example, we show the capabilities of the first PRIMA Polarimeter Imager (PPI1) filter for both the Deep and Wide surveys. We also present the number of expected photometric detections (i.e., the number of filters for which we expect to have $S/N >$ greater than the 5σ sensitivity of the survey) as a function of z, N_{H}, and L_{X} for both surveys. At the same time, we show which of these sources could be detected by *NewAthena*. As discussed in Sec. 3, our results illustrate the fraction of sources that can be detected by *PRIMA* and *NewAthena*, with the assumption that multi-wavelength coverage, SED-fitting, and spectroscopic follow-ups will correctly identify the sources as AGN and effectively constrain their bolometric luminosity. We refer to Sec. 5 for the discussion on the identification and characterization of the sources. To highlight the advancements over previous instruments, we also compare our results with the detection capabilities of *Herschel*. Specifically, we compare our predictions for the Deep survey with the values obtained by the Multi-tiered Extragalactic Surveys (HerMES)[66] survey of the COSMOS field (5σ sensitivity of 7.7 mJy at 100 μm). The Wide survey is compared with the XMM-LSS coverage from the same work (5σ sensitivity of 49.9 mJy at 100 μm). These two surveys were selected as they represent the deepest available surveys over comparable areas. The overall numbers and fractions of expected AGN are reported in Tables 2 and 3 for the Deep and Wide surveys, respectively.

We also report the AGN bolometric LFs simulated from the Deep survey with filter PPI1, and their comparison with those measured by D14 using *Herschel*-PACS data. Finally, we show the BHAD obtained by integrating the LFs and the comparison with those measured starting from X-ray or IR selections and with the values predicted by theoretical simulations.

4.1 Deep Survey

As an example of the PRIMA performance in the Deep survey, Fig. 1 illustrates the expected capabilities of *PRIMA* and *NewAthena* in detecting sources for 12 bins of L_{X} and N_{H}. The black line represents the total number of AGN in each bin per unit of redshift. The red and blue areas are the fraction of sources that we will be able to detect with *PRIMAger* PPI1 (at 98 μm) and *NewAthena* WFI, respectively. The purple area is the fraction that should be detected with both instruments. Finally, the capabilities of the *Herschel* survey of the COSMOS field are represented by the cross-hatched area.

As we can see, in this wavelength range, *PRIMA* will be able to detect almost all the AGN up to redshift 2. For $\log(L_{\mathrm{X}}/\mathrm{erg\ s^{-1}}) > 43$, we also expect to have detections up to $z \sim 4$. We can see that in this band, our ability to detect AGN depends mostly on the luminosity of the AGN rather than their obscuration. On the other hand, for *NewAthena*, we will detect most of the unobscured AGN up to $z \sim 3$ (or $z \sim 2$ for $\log(L_{\mathrm{X}}/\mathrm{erg\ s^{-1}}) \leq 42.3$) but miss most of the CT-AGN even at low

Table 2 Summary of the *PRIMA* and *NewAthena* capabilities in detecting AGN for the Deep survey. N_{AGN} is the total number of expected AGN, and WFI refers to the percentage that will be detected with *NewAthena* WFI. PHI1 and PHI2 refer to the percentage of AGN that we expect to detect with the two of the (sub-) filters of PHI (at 34 μm and 65 μm, respectively), similarly for PPI1 and PPI3 (at 98 μm and 172 μm, respectively). For both PHI and PPI, the number in parenthesis is the fraction of sources that should be visible with both *NewAthena* and *PRIMA*. $N_{filters}$ is the average number of *PRIMAger* photometric filters that each source will be detected in (only for those detected). PACS refers to the fraction of sources that would be detected by *Herschel* PACS at 100 μm for a sensitivity similar to the HerMES COSMOS survey.

		WFI	PHI1	PHI2	PPI1	PPI3		PACS
Deep survey	N_{AGN}	%	%	%	%	%	$N_{filters}$	%
All AGN	25,400	26	$35 \pm 6\,(17)$	$34 \pm 4\,(16)$	$59^{+4}_{-5}\,(23)$	$70 \pm 4\,(25)$	7	11
AGN $z \leq 4$	21,600	29	$41 \pm 7\,(20)$	$40 \pm 5\,(19)$	$36 \pm 5\,(27)$	$81^{+4}_{-5}\,(29)$	11	14
AGN $z \leq 2$	15,200	33	$52 \pm 8\,(25)$	$54 \pm 6\,(25)$	$85^{+4}_{-5}\,(33)$	$92 \pm 3\,(33)$	14	19
All CT-AGN	10,800	3	$34 \pm 7\,(3)$	$34 \pm 4\,(3)$	$61 \pm 4\,(3)$	$71 \pm 4\,(3)$	7	12
CT-AGN $z \leq 4$	9200	4	$40 \pm 8(4)$	$40 \pm 4\,(4)$	$71 \pm 5\,(4)$	$83 \pm 4\,(4)$	10	14
CT-AGN $z \leq 2$	6600	5	$49 \pm 9\,(5)$	$55 \pm 6\,(5)$	$87 \pm 4\,(5)$	$93 \pm 2\,(5)$	14	20

Table 3 Summary of the *PRIMA* and *NewAthena* capabilities in detecting AGN for the Wide survey. Columns are the same as Table 3. PACS refers to the fraction of sources that would be detected by *Herschel* PACS at 100 μm for a sensitivity similar to the HerMES XMM-LSS survey.

	N_{AGN}	WFI	PHI1	PHI2	PPI1	PPI3		PACS
Wide survey	$\times 10^5$	%	%	%	%	%	$N_{filters}$	%
All AGN	5.8	24	$11 \pm 3\,(6)$	$15 \pm 3\,(8)$	$36 \pm 4\,(15)$	$47^{+5}_{-6}\,(18)$	4	1
AGN $z \leq 4$	5.0	26	$13 \pm 3\,(7)$	$18^{+4}_{-3}\,(10)$	$43^{+4}_{-5}\,(18)$	$57^{+6}_{-7}\,(21)$	7	2
AGN $z \leq 2$	3.5	30	$19 \pm 5\,(10)$	$25 \pm 5\,(13)$	$59^{+5}_{-6}\,(25)$	$75 \pm 7\,(27)$	11	2
All CT-AGN	2.5	2	$13 \pm 3\,(2)$	$16 \pm 3\,(2)$	$37 \pm 3\,(2)$	$47 \pm 5\,(2)$	6	2
CT-AGN $z \leq 4$	2.1	3	$15 \pm 3\,(3)$	$19 \pm 3\,(3)$	$44 \pm 4\,(3)$	$55 \pm 6\,(3)$	7	2
CT-AGN $z \leq 2$	1.5	3	$21^{+4}_{-5}\,(3)$	$27 \pm 5\,(3)$	$61 \pm 5\,(3)$	$74^{+7}_{-8}\,(3)$	10	3

redshift. Where *NewAthena* shines is in detecting high-luminosity AGN, both obscured and unobscured: for $\log(L_X/\mathrm{erg\,s^{-1}}) \geq 44$ and $\log(N_H/\mathrm{cm^{-2}}) \leq 22.5$, we expect to detect all AGN up to $z \sim 6-8$. Finally, we can see that *Herschel* surveys are able to completely detect the AGN population only up to $z \sim 1$ and reveal the most luminous ones only up to $z \sim 2$.

In Fig. 2, we illustrate the expected number of *PRIMAger* photometric detections for the Deep survey. The black lines are the total number of AGN per unit of redshift for different bins of L_X and N_H. The dotted areas are the AGN fractions that we will be able to detect with *NewAthena*. The color code indicates the number of *PRIMA* filters for which we expect to have a detection. For example, dark blue sources will be detected only in one or two photometric bands, while those in yellow will have complete coverage from 24 to 235 μm. As we can see, we expect to be able to detect in all *PRIMAger* bands most of the $z \leq 2$ sources with $\log(L_X/\mathrm{erg\,s^{-1}}) \geq 43$. For AGN with lower luminosity, a complete coverage is possible only up to $z \sim 1$. However, we expect to be able to reveal all the AGN in at least a couple of filters up to $z \sim 2$, effectively covering all the sources at the "cosmic noon." As most of the AGN lies at

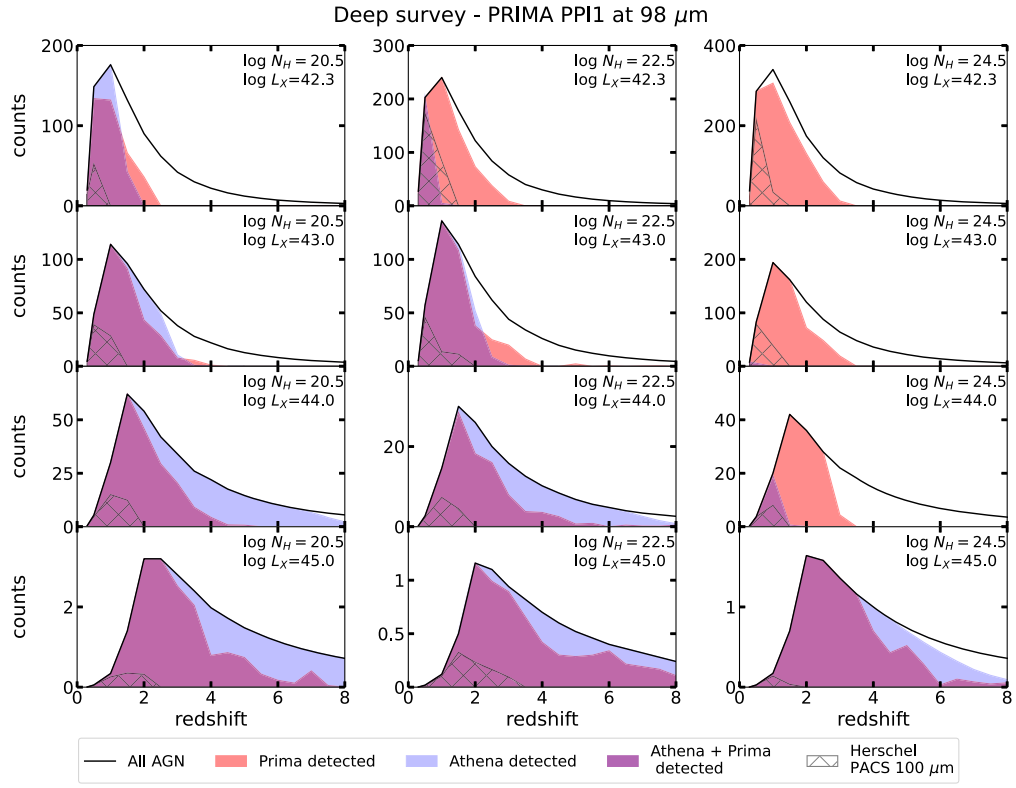

Fig. 1 Number of AGN expected per unit of redshift ($\Delta z = 1$) for the *PRIMA* Deep survey. The black lines are the total number of expected AGN, the red areas represent those that can be detected with the *PRIMAger* PPI1 at 98 μm, the blue areas those which can be detected in the X-rays with the *NewAthena* WFI, the purple areas are the AGN that will be detected by both instruments. For comparison, we reported (cross-hatched area) the performance of *Herschel* PACS at 100 μm for a survey similar to the HerMES survey of the COSMOS field. The columns refer to AGN with different amounts of obscuration (from left to right, $20 \leq \log(N_{\rm H}/{\rm cm}^{-2}) \leq 21$; $22 < \log(N_{\rm H}/{\rm cm}^{-2}) \leq 23$; $24.18 < \log(N_{\rm H}/{\rm cm}^{-2}) \leq 25$) and the rows to different AGN luminosity (from top to bottom, $42.0 \leq \log(L_{\rm X}/{\rm erg\,s}^{-1}) < 42.3$, $42.9 \leq \log(L_{\rm X}/{\rm erg\,s}^{-1}) < 43.2$, $43.9 \leq \log(L_{\rm X}/{\rm erg\,s}^{-1}) < 44.2$, $44.9 \leq \log(L_{\rm X}/{\rm erg\,s}^{-1}) < 45.2$).

$z \leq 3$, we expect *PRIMA* to detect ~30% of all AGN in all the 16 bands and more than 70% in at least one band. Furthermore, we should be able to detect most AGN with $\log(L_{\rm X}/{\rm erg\,s}^{-1}) \geq 44$ in one or two photometric filters up to $z \sim 4$, with some detections expected up to $z \sim 6$. Finally, we stress that for the sources with a low number of filter detections but visible with *NewAthena*, the latter will allow us to recognize these sources as AGN and to put constraints on their properties (i.e., obscuration and intrinsic luminosities). On the other hand, multi-wavelength coverage, SED-fitting, and spectroscopic follow-ups can be exploited to fully characterize the sources without *NewAthena* detections (i.e., heavily obscured and low-luminosity AGN, see Sec. 5).

A summary of the Deep survey performances of four of the *PRIMAger* filters, as well as of *NewAthena* and *Herschel* is reported in Table 2.

4.2 Wide Survey

Similarly to Sec. 4.1, we show the expected performance of *PRIMAger* PPI1 for the Wide survey in Fig. 3. We used the same color code as Fig. 1, with the difference that the considered area (thus the AGN expected number) is 28 times larger.

As we can see, the capability of detecting high-z AGN decreases significantly with respect to the Deep survey. In particular, we will be able to detect all the AGN only up to $z \sim 1$, or $z \sim 2$ for those with $\log(L_{\rm X}/{\rm erg\,s}^{-1}) \geq 44$. On the other hand, the decrease in depth for *NewAthena* is not so impactful. This is due to the *NewAthena* sensitivity limit between the two surveys decreasing only by a factor $\sqrt{2/3}$. Similarly to the Deep survey, *NewAthena* on its own is not able to detect

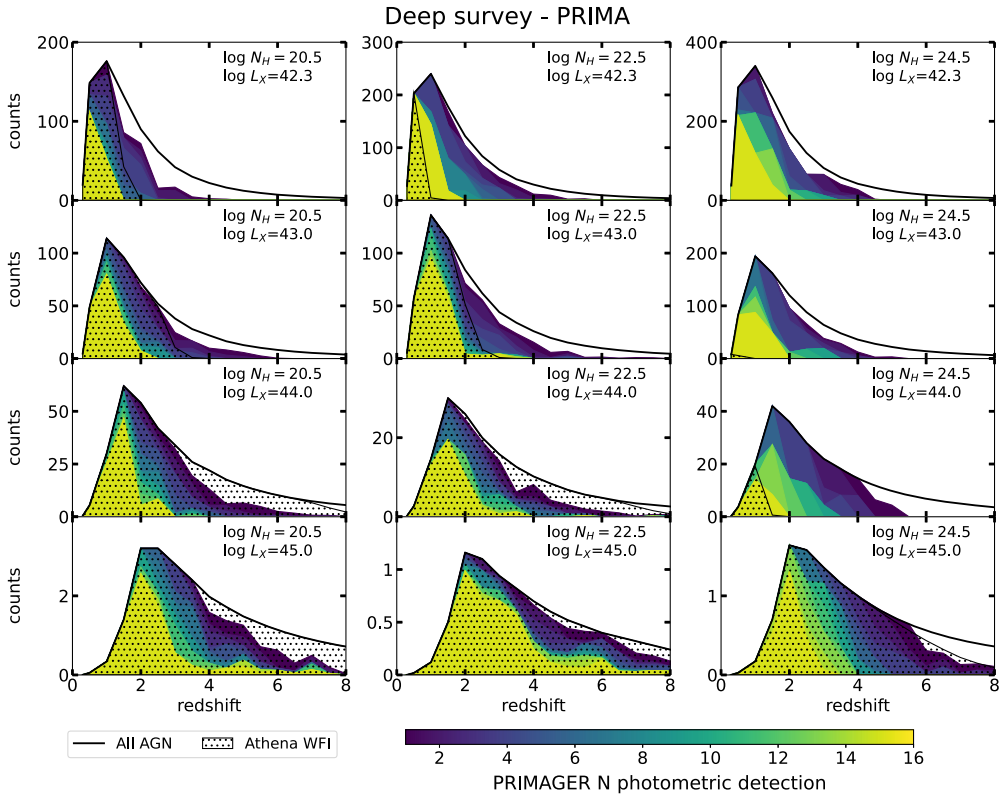

Fig. 2 Expected number of photometric detection per unit of redshift for the *PRIMA* Deep survey. The solid black lines represent the total number of expected AGN, whereas the dotted regions highlight those that will be detected in X-rays using the *NewAthena* WFI. The color coding illustrates the number of *PRIMAger* filters capable of detecting these sources. Specifically, the yellow areas correspond to AGN detected across all filters, i.e., complete detections with both *PRIMA* PHI and PPI. By contrast, the dark blue regions represent sources expected to be detected in only one or two filters. Columns and rows follow the same scheme as in Fig. 1.

the majority of the CT-AGN (with the exception of the most luminous) and struggles with the obscured ($N_{\rm H} \geq 10^{22.5}$ cm^{-2}) low-luminosity ones ($L_{\rm X} \leq 10^{42.3}$ erg/s). Finally, we want to highlight that due to the large area (thus lower sensitivity), very few sources are detected by *Herschel* PACS above $z \sim 0.5$.

Despite the lower detection fractions, the Wide survey can take advantage of its 28 deg^2 area to significantly boost the number of detected AGNs. In particular, this survey can be extremely effective in revealing the rarest sources. For example, although we will not be able to detect all the AGN with $\log(L_{\rm X}/{\rm erg\,s^{-1}}) \sim 44$ and $\log(N_{\rm H}/{\rm cm^{-2}}) \sim 22.5$ (even those at $z \sim 2$), we still expect to find ∼14,000 of them, a significant improvement over the ∼1,200 that the Deep survey will reveal. This is also evident in the number of expected detections of CT-AGN: although the Deep survey should reveal ∼7000 of them, the Wide survey, mostly limited to $z \leq 2$, should boost this number by a factor ∼10.

In Fig. 4, we illustrate the expected number of *PRIMAger* photometric detections for the Wide survey. We used the same color code as in Fig. 2. As we can see, we will be able to take advantage of all the bands only up to $z \sim 1$, except for some of the most luminous AGN that we can be detected up to $z \sim 2$. However, for the $z \leq 4$ and $z \leq 2$ sources that will be revealed (which should be more than 100,000), we expect on average detections in seven and 11 *PRIMAger* bands, respectively. Furthermore, as the differences between the depth of the Deep and Wide survey of *NewAthena* are minimal, we will be able to take advantage of the *NewAthena* detections to characterize the sources. In fact, with the exception of the most obscured sources and those with very low luminosities, most of the AGN with a couple of *PRIMA* photometric detections will also be revealed by *NewAthena*. We refer to Sec. 5, for a discussion on the characterization of AGN lacking *NewAthena* detections. We report in Table 3 a summary of the *PRIMA*

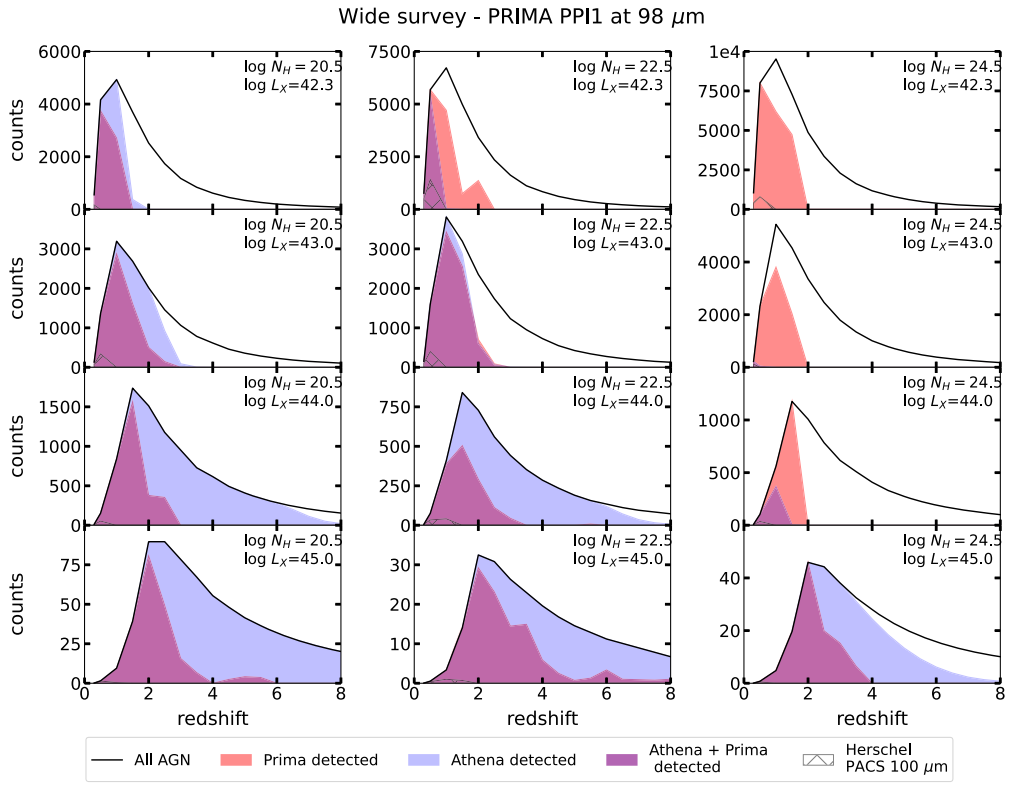

Fig. 3 Number of AGN expected per unit of redshift for the *PRIMA* Wide survey with PPI1. The lines and areas are coded as in Fig. 1.

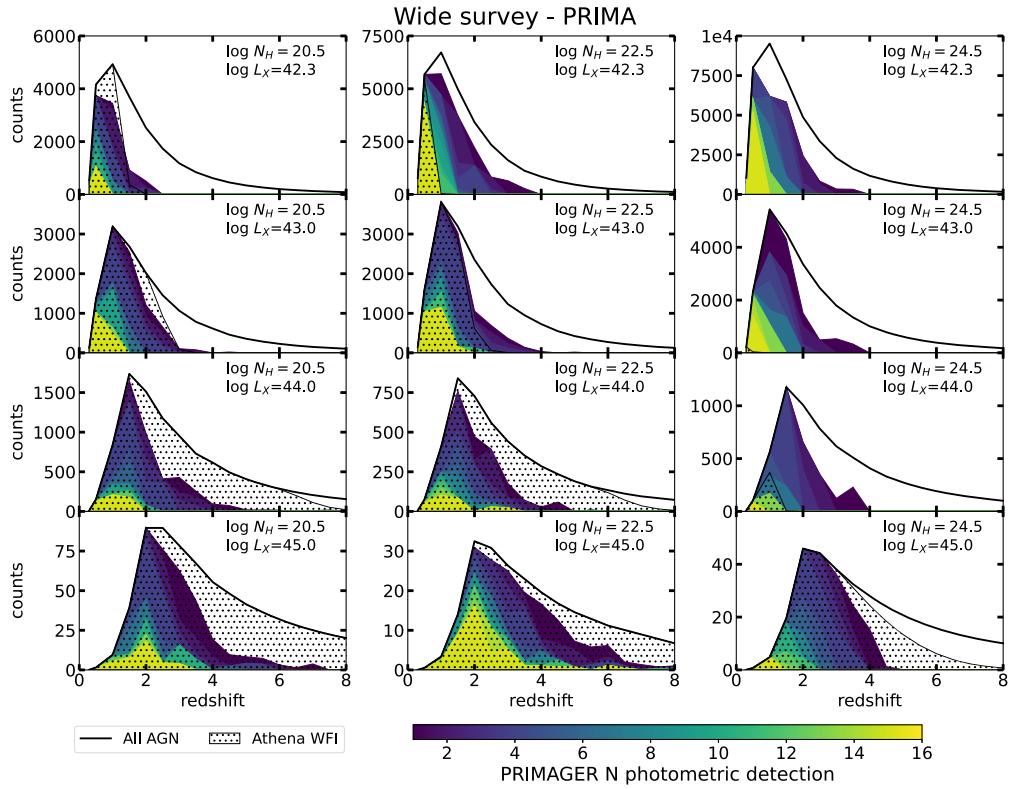

Fig. 4 Expected number of photometric detection per unit of redshift for the *PRIMA* Wide survey. The lines and areas are coded as in Fig. 2.

and *NewAthena* predictions for a Wide survey, as well as the comparison with *Herschel*'s capabilities.

4.3 Black Hole Accretion Rate Density Evolution

Adopting the method described in Sec. 3.2, we were able to fit the LFs up to $z = 8$. In Fig. 5, we show the LFs obtained from PPI1 simulations in different z bins. The error bars represent 1σ Poisson uncertainties.[67] The black line indicates our best-fit LFs, with the associated uncertainties (derived through random sampling of the SEDs; see Sec. 3.2) shown as a hatched black area. For comparison, the orange line and shaded area denote the best-fit LF and its uncertainties derived by D14. The red-shaded region highlights the bolometric luminosity range accessible through current X-ray surveys,[18,20,21] assuming an L12 bolometric correction. Due to the low number of sources in the $7 \leq z < 8$ bin, we fixed the L^* to the best-fit value found at $5 \leq z < 6$. We report in Table 4 the bolometric LF best-fit values and their 1σ uncertainties.

Our LF results are consistent with those of D14 across all redshift bins. The most significant differences are seen in the lowest redshift bin, where we have fewer sources at the bright end of the LF and small uncertainties. These small uncertainties are mainly driven by two factors: first, *PRIMA* detects almost all the sources in the entire redshift bin; thus, there is little difference in extracting one SED or another; second, we expect ∼1000 sources but have only 400 SEDs at our disposal; thus, the variations when bootstrapping are minimal.

We further examined the points showing the largest deviation from our LF best fit (e.g., $\log(L_{\rm bolo}/{\rm L}_\odot) \sim 12$ at $0.7 \leq z < 1.2$ and $\log(L_{\rm bolo}/{\rm L}_\odot) \sim 11 - 12$ at $2.5 \leq z < 3.8$). Their

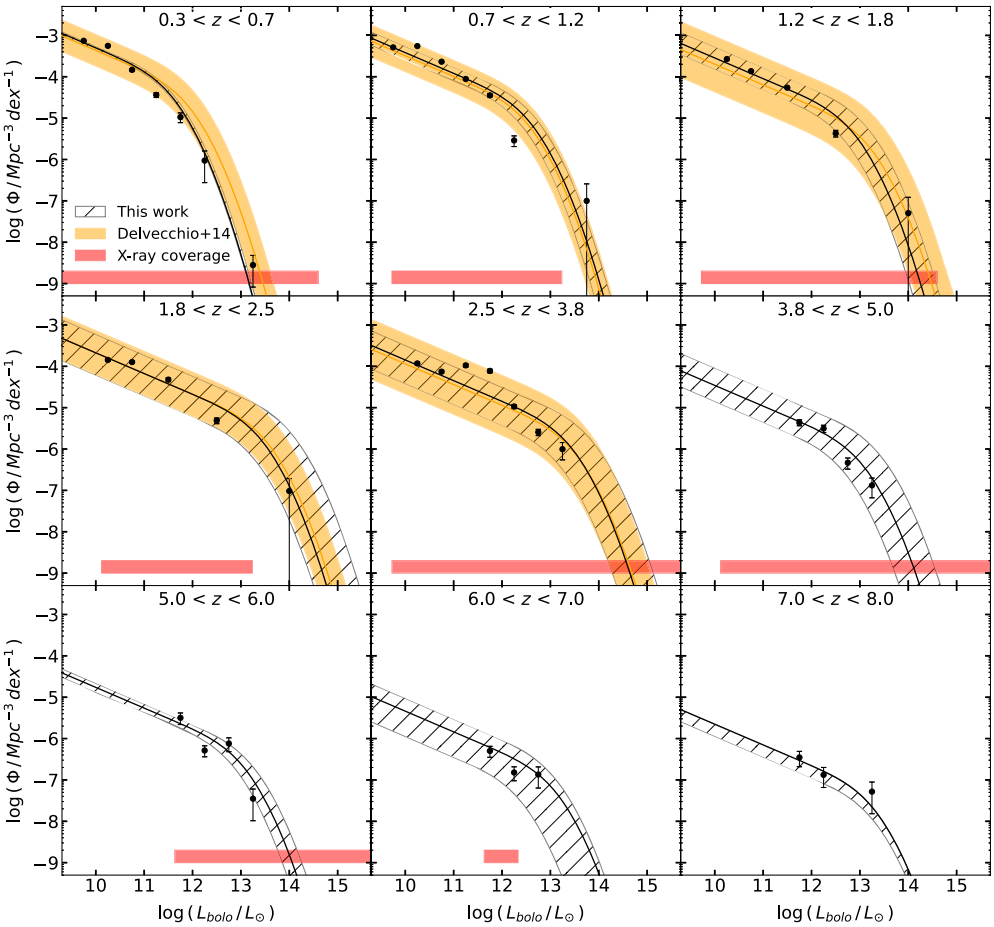

Fig. 5 AGN bolometric luminosity function expected from a *PRIMA* Deep survey with PPI1 (98 μm). The black line is our best-fit and the shaded area represents its uncertainties. The orange line is the best-fit LF derived from *Herschel*-PACS data by D14.[32] The red areas highlight the bolometric luminosity range covered by current X-ray surveys.[18,20,21]

Table 4 List of best-fit parameters of the AGN bolometric LFs and associated uncertainties. We fitted the LFs with modified Schechter functions, fixing the faint- and bright-end slopes to the values of D14, i.e., $\alpha = 1.48$ and $\sigma = 0.54$. For the $7 \geq z < 8$ bin, due to the low number of degrees of freedom, we also fixed the luminosity at the knee of the LF at the values of the previous bin.

z bin	$\log(L^*/L_\odot)$	$\log(\Phi^*/\mathrm{Mpc}^{-3}\,\mathrm{dex}^{-1})$
$0.3 \leq z < 0.7$	$11.00^{+0.04}_{-0.01}$	$-3.8^{+0.03}_{-0.05}$
$0.7 \leq z < 1.2$	$12.0^{+0.1}_{-0.2}$	$-4.36^{+0.09}_{-0.08}$
$1.2 \leq z < 1.8$	$12.2^{+0.3}_{-0.2}$	$-4.87^{+0.12}_{-0.18}$
$1.8 \leq z < 2.5$	$12.2^{+0.6}_{-0.1}$	$-4.9^{+0.1}_{-0.5}$
$2.5 \leq z < 3.8$	$12.9^{+0.4}_{-0.2}$	$-5.3^{+0.1}_{-0.5}$
$3.8 \leq z < 5$	12.6 ± 0.4	-5.9 ± 0.2
$5 \leq z < 6$	12.2 ± 0.2	-6.0 ± 0.1
$6 \leq z < 7$	$12.7^{+0.2}_{-0.7}$	-6.5 ± 0.3
$7 \leq z < 8$	12.7	$-0.7^{+0.1}_{-0.3}$

behavior can be attributed to the binning used in computing the LF. In particular, it arises from simulating the expected number of sources and the survey completeness (see Sec. 3) in quite large L_X and z bins that do not exactly match the L_{bolo} and z binning used to compute the LF.

In Fig. 6, we demonstrate the capabilities of *PRIMA* in measuring the BHAD. The black points are our simulated measures of the BHAD obtained by integrating the LFs (see Sec. 3.2). For comparison, the red-shaded area represents measured BHAD values from X-ray-selected galaxies.[18–21,68] Predictions from various simulations are shown as a blue-shaded region,[69–71] whereas the orange-shaded area and points correspond to BHADs measured from *Herschel*-PACS selected sources in D14 and JWST-selected sources,[23] respectively. Up to $z \sim 3$, our predictions align with the BHAD values from D14 and are consistent with those measured via X-ray observations. At $z > 3$, our BHAD estimates follow the trends observed in X-ray surveys, which is expected as our simulations started from X-ray background modeling. The smaller uncertainties at $7 \leq z < 8$ (with respect to the previous bin) arise from fixing the L^* in fitting of the LF.

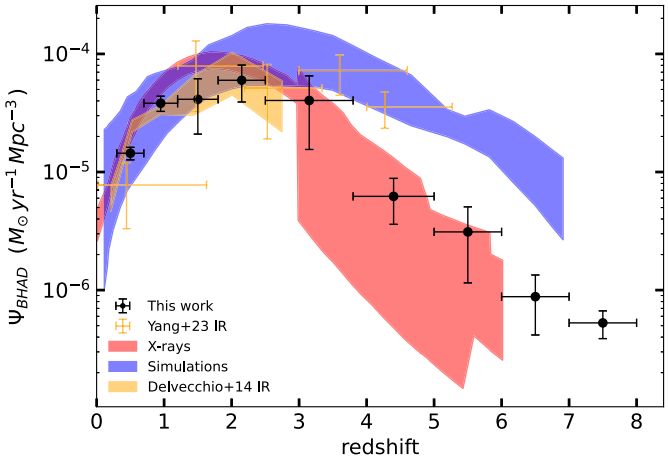

Fig. 6 Prediction of *PRIMA*-derived measurements of the BHAD. The black points represent the predictions of the BHAD obtainable with a *PRIMA* Deep survey with PPI1 (98 μm). For comparison, we report the BHAD measured from X-ray surveys (red area)[18–21,68] and IR surveys (orange area and points).[23,32] In blue, BHAD predictions from simulations[69–71] are shown. Our points follow the BHAD measured from the X-rays as our simulations started from X-ray background modeling.

Regardless of the simulated BHAD values at high redshifts, we find that with *PRIMA*, we will be able to measure the evolution of the BHAD up to $z \sim 8$ with reasonable accuracy. As a sanity check, we utilized the SPRITZ simulations of Bisigello et al. (2024, hereafter B24)[47] to evaluate the capabilities of *PRIMA* in measuring the BHAD. Briefly, SPRITZ derives the number densities of star-forming galaxies, AGN, and composite objects up to $z = 10$ from the IR LFs of these populations. The simulated IR luminosity range spans between $L_{IR} = 10^5\,L_\odot$ and $L_{IR} = 10^{15}\,L_\odot$. Each object in the simulation is assigned a SED model based on its classification, which is then used to derive fluxes in various bands. For further details, we refer to B24. We used the same approach of Sec. 3.2 to measure the bolometric LFs and BHAD derived from the 100 μm detections. We found that *PRIMA* is able to recover more than 90% of the simulated BHAD at $z \geq 1$ and up to $z \sim 8$. The BHAD simulated with SPRITZ is systematically higher than that obtained from our simulations and remains nearly constant at $z > 3$, similar to JWST-measured BHAD.[23] Due to the intrinsically higher BHAD predicted by SPRITZ, its measurements exhibit even smaller uncertainties than those from our simulations: ~5% at $z \leq 3$, ~10% at $4 \leq z \leq 6$, and ~35% at $z \geq 7$. It is important to emphasize that, regardless of the actual evolution of the BHAD, the objective of this work is to demonstrate that *PRIMA* will be capable of measuring it with reasonable accuracy. Given that the source number densities in B24 are derived from IR LFs rather than from the XRB as in our work, and that different SED models were employed, our findings provide strong evidence that *PRIMA* will effectively be able to measure the BHAD at high redshifts.

5 Discussion

Our simulations of the capabilities of *PRIMA* and *NewAthena* are reported in Sec. 4 and summarized in Tables 2 and 3. Figure 6 shows *PRIMA*'s capabilities in reconstructing the evolution of the BHAD. In this section, we discuss the synergies between the two instruments, the improvements over existing surveys, and the huge importance that FIR observatories such as *PRIMA* will have in the next decades.

As shown in Figs. 1 and 3, the two layers of the *PRIMA* survey strategy (1000 h covering 1 deg^2 and 1000 h covering 27 deg^2) complement each other effectively. The Deep layer will detect nearly all AGN up to $z \sim 2$ (at least down to $\log(L_{\rm bolo}/{\rm erg\,s^{-1}}) \sim 43$, i.e., the lower limit in our simulations) and will detect sources up to $z \sim 4$ and beyond (those with $\log(L_{\rm bolo}/{\rm erg\,s^{-1}}) \geq 45$), providing excellent (and, for sources with $\log(L_{\rm bolo}/{\rm erg\,s^{-1}}) \geq 45.5$, nearly complete) coverage of the "cosmic noon." Meanwhile, the Wide survey, with its large area, will excel in the number of detectable sources. We expect to detect up to $\sim 3 \times 10^5$ AGN in total with $\log(L_{\rm bolo}/{\rm erg\,s^{-1}}) \sim 43.3$, of which about 30,000 with complete detections across all 16 *PRIMAger* bands. Multiple detections across various bands are critical for two reasons. First, shorter wavelength detections can help resolve sources that are blended at longer wavelengths, a technique successfully demonstrated using both *Spitzer* and *Herschel* observations,[72,73] as well as *PRIMA* simulations.[52] Second, in the absence of spectroscopic data, the most effective way to characterize a source and derive its properties is through SED fitting, and *PRIMA* will excel at it.[47] Given the degeneracies between AGN and host-galaxy models and their intrinsic uncertainties, the ability to separate the two components is directly linked to the number of photometric detections. Currently, the best FIR coverage comes from *Spitzer* and *Herschel*, but for most sources at $z \sim 1$ and beyond, there are typically only one or two photometric detections. *PRIMA*, with its 16 contiguous filters, will be a game changer in the SED-fitting of high-z objects. Figure 11 of B21[56] demonstrates the improvement in constraining the AGN and host galaxy properties provided when incorporating four additional FIR filters. B24 showed that we can effectively recognize AGN using the *PRIMA* coverage to measure the shape of the IR dust continuum. B24 simulated *PRIMA* observations of "normal" and active galaxies over a large range of AGN fractions, IR luminosities, PAH contribution, dust properties, and redshifts and performed SED-fitting to investigate *PRIMA* capabilities in recovering the source properties. In particular, exploiting PHI, PPI1, and PPI2 filters, B24 was able to retrieve the AGN fraction with a dispersion of 0.06, the fraction of dust mass in PAH with a precision of ~10%, and the IR luminosity with a scatter of 0.1 dex.

In addition, most of the obscured AGN emission is usually in the $5-30$ μm (rest-frame) band coinciding with the wavelength range where PAH and dust emission from the host galaxy are also present. Properly disentangling these components requires both good coverage at these wavelengths and longer-wavelength photometric detections to constrain the host-galaxy dust emission, both of which will be provided by *PRIMA*. Although current facilities such as JWST cover up to 28 μm (albeit JWST is not ideal for large-area surveys), much of the obscured AGN emission is shifted out of its bands for $z \geq 1$. By contrast, *PRIMA*'s continuous coverage from 24 to 250 μm can trace the AGN emission up to $z \sim 10$ and beyond, and its ability to detect high-z AGN will mainly depend on the survey depth.

To accurately reconstruct the BHAD, it is essential not only to identify sources as AGN but also to precisely measure their bolometric luminosities. Therefore, we further assessed our ability to recover AGN and host-galaxy properties through SED-fitting. Following the methodology of B24, we used CIGALE to simulate observations of high-redshift AGN. We considered six redshift bins with $1 \leq z \leq 6$, generating 1280 SEDs per redshift bin. These SEDs encompass a range of star formation histories, stellar ages, AGN fractions, and AGN inclinations. Specifically, we simulated sources with stellar masses of $M_* = 5 \times 10^{10}$ and 5×10^{11} $M_\odot$, star formation rates $\log(SFR/M_\odot\ \mathrm{yr}^{-1}) \in [-5,4]$, and bolometric luminosities $\log(L_{\mathrm{bolo}}/\mathrm{erg\,s}^{-1}) \in [43,48]$. We then performed SED fitting on the simulated observations and compared the recovered properties with the intrinsic values used to generate them. The simulated observations were designed to resemble real deep-field surveys. The optical-NIR coverage is identical to that of the COSMOS 2020 catalog,[74] whereas the mid- and far-IR data are modeled after the XID+ deblended catalog.[73] For each band, we adopted a sensitivity corresponding to the median uncertainties of the sources in these catalogs. In addition, we simulated *PRIMA* PHI and PPI observations, incorporating uncertainties equivalent to the 1σ survey sensitivity. Gaussian noise, with a standard deviation matching the band uncertainty, was added to all photometric fluxes. The left and center panels of Fig. 7 present the normalized distribution of the difference between the SED-fitting derived and true values for the SFR and the L_{bolo}. We examine three scenarios: (i) without mid- and far-IR coverage (a common situation for $z > 3$), (ii) including *PRIMA* coverage, and (iii) incorporating *PRIMA*, along with *Spitzer* and *Herschel* data. Notably, complete wavelength coverage does not necessarily imply detections in all bands; if the flux plus noise fell below the band sensitivity threshold, the corresponding photometric point was treated as a non-detection. We found that with *PRIMA* coverage we can recover (within 0.1 dex of the true value) the bolometric luminosity for 75% of our sources and for 63% of those at $z \geq 3$, a significant improvement over the $18-20$% of the sources without mid-IR and far-IR coverage. We also expect *PRIMA* to double the number of sources with reliable SFR (within 0.1 dex of the true value), with the fraction increasing from ∼32% to 63%. We run further simulations focusing on sources at $6 \leq z \leq 8$. We found that using *PRIMA* photometric bands, we measure bolometric luminosity within 0.1 dex of the true value for ∼30% of the simulated objects. More importantly, for the majority of sources with $\log(L_{\mathrm{bolo}}/\mathrm{erg\,s}^{-1}) \geq 45$, the measured L_{bolo} is within 0.3 dex of the true value. Specifically, for sources with $45 \leq \log(L_{\mathrm{bolo}}/\mathrm{erg\,s}^{-1}) < 46$, we obtain an average offset of $\log L_{\mathrm{bolo}}^{\mathrm{sed}} - \log L_{\mathrm{bolo}}^{\mathrm{true}} = 0.24 \pm 0.30$, similar to the Bayesian uncertainties associated to the measured values. Considering the last two redshift bins in Fig. 5 ($6 \leq z < 7$ and $7 \leq z < 8$), we can see that all the bolometric luminosity bins that we are able to populate with *PRIMA* are at $\log(L_{\mathrm{bolo}}/L_\odot) \geq 11.5$ or equivalently to $\log(L_{\mathrm{bolo}}/\mathrm{erg\,s}^{-1}) \geq 45$. Therefore, we are confident that *PRIMA* will not only be able to detect sources up to $z \sim 8$ but also to measure their L_{bolo} with reasonable accuracy, enabling us to reconstruct the bolometric LFs and BHAD even at these high redshifts.

Regarding *NewAthena*, as its first two layers have similar depths (with $t_{\mathrm{field}} = 300$ and 200 ks, respectively), the fractions of sources detected by the Deep and Wide surveys differ only by some percent. In general, we expect *NewAthena* to detect ∼25% of all the AGN and over 30% of those at $z \leq 2$. In particular, *NewAthena* will be extremely powerful in detecting moderate-luminosity AGN up to $z \sim 6$ and high-luminosity ones up $z = 8$ and beyond. For unobscured low-luminosity AGN, *NewAthena* should be able to detect all of them up to $z \sim 1$ and most of them at $z \sim 2$. However, in Fig. 2, it is easy to see that the capabilities of *NewAthena* are heavily affected by the source intrinsic obscuration. Although it can reveal AGN with $\log(N_{\mathrm{H}}/\mathrm{cm}^{-2}) \sim 20.5$ and $\log(L_{\mathrm{X}}/\mathrm{erg\,s}^{-1}) \sim 42.3$ up to $z \sim 2$, if we increase the obscuration

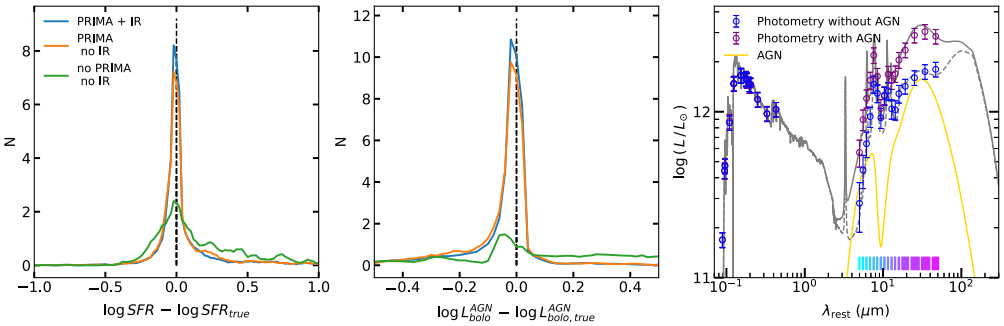

Fig. 7 *Left* and *center panels*: Normalized distribution of the difference between the estimated and the true values of the SFR and AGN bolometric luminosity. The blue lines show the result from the SED fitting using all the available filters; the orange lines represent those using only the *PRIMA* PHI and PPI bands. Finally, the green lines show the results for sources without any mid- and far-IR detection. *Right panel*: Example SEDs of a galaxy with and without an AGN. The grey dashed line represents the total SED of a non-active galaxy at $z \sim 4$ with $\log(M_*/\mathrm{M}_\odot) = 10.1$ and $SFR = 150\,\mathrm{M}_\odot\,\mathrm{yr}^{-1}$. The solid gray line corresponds to a similar galaxy hosting an AGN with $\log(L_{\mathrm{bolo}}/\mathrm{erg\,s}^{-1}) = 45.6$, whose contribution is shown by the yellow line. Simulated photometric points, including *CFHT*, *MegaCAM*, *SUBARU*, *Vista*, *Spitzer/IRAC*, and *PRIMA* filters, are displayed in blue (without AGN) and purple (with AGN). The color bar at the bottom indicates the wavelength coverage of *PRIMA* PHI and PPI bands. Despite the AGN having lower flux compared with the host galaxy dust emission in most *PRIMA* bands, the extensive coverage of *PRIMA* enables to effectively separate the two contributions, allowing for an accurate measurement of the AGN bolometric luminosity.

to $\log(N_{\mathrm{H}}/\mathrm{cm}^{-2}) = 22.5$, we are not able to go beyond $z \sim 1$. The difficulty in detecting heavily obscured AGN is easily noticeable for CT-AGN: at high-z, *NewAthena* can reveal only the most luminous, those with $\log(L_{\mathrm{X}}/\mathrm{erg\,s}^{-1}) \leq 44$ are not visible above $z \sim 1.5$, and AGN with moderate and low luminosity ($\log(L_{\mathrm{X}}/\mathrm{erg\,s}^{-1}) \leq 43$) will be completely missed. As low- and moderate-luminosity AGN comprises most of the CT-AGN population, the fraction of *NewAthena* detections of CT-AGN is only 2% to 3%.

The synergies between *NewAthena* and *PRIMA* are particularly significant in the study of obscured and CT-AGN. Many CT-AGNs that will remain undetected by *NewAthena* will likely be observed by *PRIMA* (at least up to $z \sim 3$). These CT-AGNs are expected to play a crucial role in the evolution of the BHAD and may help resolve the gap between the measured BHAD and theoretical predictions from simulations. Currently, most BHAD estimates are derived from X-ray surveys and, as such, suffer from obscuration. Even with the advanced capabilities of next-generation X-ray observatories such as *NewAthena*, a large portion of CT-AGN will remain undetected without complementary surveys in the FIR, such as those provided by *PRIMA*. The excellent capability of *PRIMA* to recover the BHAD at very high redshifts is clearly demonstrated in Fig. 6. Conversely, X-ray coverage of FIR-detected sources will be essential for characterizing these objects and distinguishing between obscured AGN and dusty SF galaxies. *NewAthena* will provide both imaging and spectroscopy, enabling constraints on key X-ray properties, including L_{X} (and consequently AGN bolometric luminosities) and N_{H}. In addition, the intrinsic X-ray luminosity (i.e., corrected for the obscuration) can be fed to SED-fitting codes to enhance our ability to accurately fit the optical and IR regimes and separate the AGN and host-galaxy contributions. Because *NewAthena* and *PRIMA* should fly within the same timeframe, it is not unreasonable to expect a coordinated survey strategy that will fully exploit the synergies between these two instruments.

The improvement of *PRIMA* over existing surveys is easily seen in Fig. 2 and even more in Fig. 4. From our simulations, the *Herschel* survey of the COSMOS field reached sensitivity that allowed us to detect ∼10% of all the AGN and ∼20% of those at $z \leq 2$. At the same band (∼100 μm), the *PRIMA* Deep survey is expected to reveal ∼60% of all AGN and ∼85% of those at $z \leq 2$. In addition, ∼30% of all AGN should have complete detection in all 16 *PRIMAger* bands. *PRIMA* will not only detect all of the AGN at the redshifts that *Herschel* was able to reach, but it will also push its detections well beyond the "cosmic noon." Therefore, the number

of detected AGNs is expected to improve by a factor 3–8. The improvement is even stronger when considering the Wide survey. For such a survey, *Herschel* was not able to detect more than 1% to 2% of the AGN populations, whereas *PRIMA* will reveal between ∼10 and ∼50%. Summarizing, regarding galaxy evolution and AGN, *PRIMA* can be considered a true successor of *Herschel*: it will sample a similar parameter space but with better sensitivity and more photometric bands, thus allowing us to characterize the entire population of the sources detected by *Herschel* and to reach redshifts that were not possible before.

Regarding the BHAD, our simulations demonstrate that *PRIMA* will be able to measure it up to $z \sim 8$, regardless of the BHAD assumed in this work and of the SED utilized. Prior to the advent of JWST, the deepest IR-derived BHAD measurements extended only to $z \sim 3$. Currently, we are able to measure it up to $z \sim 4-5$, though JWST is not ideal for conducting large-area surveys. With current X-ray surveys, we can measure the BHAD up to $z \sim 6$; however, a major challenge is correcting for the contribution of the most obscured AGN, which is mostly missed by X-ray selections. As already discussed, *PRIMA* detection capabilities do not depend on the source obscuration and its completeness is mostly dominated by the source fluxes, making it far easier to compute. Our simulations show that *PRIMA*'s capabilities in measuring the BHAD will exceed any current IR or X-ray instrument. With *PRIMA*, we will be able to explore the BHAD at previously inaccessible redshifts and address long-standing questions, such as whether the gap between X-ray-derived BHAD estimates and theoretical predictions is caused by the contribution of highly obscured AGN.

Accurately measuring the BHAD across cosmic times not only enables the study of black hole accretion mechanisms and feedback processes but could also provide a potential test for the dark energy content of the Universe. As the local SMBH function must be equal to the integral of the AGN accretion across cosmic times plus the total mass increase due to cosmological coupling (i.e., the BH mass growth due to the cosmological expansion), knowing the BHAD evolution and the local SMBH would allow us to measure the cosmological coupling. The latter could provide insight on the equation of state of the matter inside the BH and on their possible contribution to the dark energy content of the Universe.[75–77]

Although we compared our BHAD predictions with those derived from X-ray and infrared surveys, as well as with estimates from cosmological simulations, recently, there have been attempts to measure it starting from JWST detections of dust-reddened broad-lines AGN, commonly referred to as "Little Red Dots" (LRDs).[78] The AGN nature LRDs is still a matter of discussion, with alternatives comprising compact dust-rich star-forming galaxies, brown dwarfs, or other more exotic sources,[79–82] assuming an AGN origin leads to $z \sim 6-8$ BHAD measurements that exceed any of the previous of at least one order of magnitude.[83] This additional discrepancy further strengthens the critical need for accurately measuring the BHAD at high-z. Our predictions of the BHAD are inherently dependent on the assumptions we made in our simulations. In particular, on the total number of expected AGN and its redshift evolution, which we based on the XRB modeling. As discussed in Sec. 4.3, assuming a different BHAD does not impact significantly our capability of recovering it via *PRIMA* surveys. Although the exact values of the BHAD depend on the assumed distribution of AGN and their evolution, the uncertainties associated with our simulation do not. Instead, they reflect the intrinsic BHAD uncertainties measurable with *PRIMA*. The legacy value of this work is in showing that *PRIMA* will allow us to measure the BHAD with better accuracy than current IR and X-ray surveys, up to higher redshift than what is now possible, and free from obscuration biases.

To facilitate direct comparisons with PACS-derived BHAD measurements, this work has focused on demonstrating *PRIMA* capabilities in measuring the BHAD specifically starting from a 100 μm survey. We want to highlight that *PRIMAger* will observe simultaneously across its entire wavelength range, from 24 to 261 μm, offering several advantages. First, lower-frequency detections with *PRIMAger* can be used as priors to deblend sources at longer wavelengths, ensuring more reliable flux measurements.[52] Second, as discussed previously, it will allow us to characterize the host galaxy and AGN properties, facilitating robust AGN identification.[47,56] Finally, having contemporary surveys at all *PRIMA* wavelengths will allow us to merge those to increase the number of detected AGNs. This is particularly critical for identifying obscured AGN in quiescent or faint-FIR galaxies that may remain undetected at 100 μm. The increased AGN sample will simplify the incompleteness corrections, further reducing the BHAD uncertainties.

Characterizing newly discovered sources will strongly depend on accurately constraining their redshifts. Although reliable photometric redshifts should be achievable for AGN detected across all *PRIMAger* bands, sources with a low number of photometric detections will require spectroscopic follow-ups. However, as in the next decades, we expect a huge number of new objects to be revealed by telescopes such as LSST, SKAO, CTA, and the Nancy Grace Roman Space Telescope, new facilities and surveys dedicated to efficiently provide spectroscopy are also being developed. In particular, the *PRIMA* surveys could be conceived to cover fields that will have complete deep spectroscopic coverage at the time of its launch. For example, in the next years, the COSMOS, GOODS, and Euclid Deep Fields will receive spectroscopic coverage from 4MOST. The Wide-Area VISTA Extragalactic Survey (WAVES) and the Optical, Radio Continuum, and HI Deep Spectroscopic Survey (ORCHIDSS) will target more than 180,000 galaxies in these fields. In addition, *PRIMA* could benefit from planned facilities like the Wide Field Spectroscopic Telescope (WFS), which is expected to deliver $R = 3000 - 4000$ Multi-object spectroscopy for 250 million sources, along with over 4 billion spectra via its $R = 3500$ integral field spectrograph.[84]

Finally, we highlight that although its investigation exceeds the scope of this work, *PRIMA* will also carry on board a pointed spectrometer (*FIRESS*) covering the $24 - 235$ μm wavelength range and able to operate in low- ($R \sim 100$) and high-resolution ($R \sim 4400 - 12{,}000$) modes. In the case of sources with few photometric detections and not visible by *NewAthena* (e.g., most of CT-AGN), characterizing these sources and constraining their host-galaxy and AGN properties will benefit from follow-ups with *FIRESS*. In particular, AGN-related high-ionisation lines, such as [Ne V] 14.3 μm and 24.3 μm, [O IV] 25.9 μm,[85–87] and the 9.7 μm and 18 μm silicate features will fall within the *FIRESS* wavelength coverage. The 9.7 μm feature is typically associated with unobscured AGN when observed in emission and with obscured ones when it is in absorption. Moreover, its depth has been shown to correlate with the X-ray derived N_H.[88–90] To quickly illustrate the capability of FIRESS in performing follow-up observations of AGN detected by *PRIMAger*, we utilized $L_{bol} - L_{line}$ relations to estimate the fluxes of the [Ne V] 14.3 μm and 24.3 μm, [O IV] 25.9 μm emission lines of our sources.[91] Assuming the Wide survey sensitivity and a signal-to-noise ratio threshold of 5, we found that a total observing time of ~24 hrs is sufficient to detect the 10 most luminous sources at $z > 2$ in all three emission lines. At $z > 4$, detecting the 10 most luminous AGNs with both [Ne V] 14.3 μm and [O IV] 25.9 μm requires ~90 h of integration time. Finally, considering only [O IV] detections, the 100 most luminous AGN at $z > 2$ can be detected in ~150 h. For a more detailed analysis of the use of AGN- and star formation-related emission lines in characterizing AGN and host-galaxy properties, we refer to B24.

Besides AGN-related lines, we also expect to detect the SF-related polycyclic aromatic hydrocarbon (PAH) features,[92] as well as fine structure lines of O, C, Ne, S, N, Fe, Ar, and Si that can be used to probe the neutral and ionized gas and to estimate redshift, amount of gas, the contribution of AGN and SF to the continuum emission, and the presence of outflows.[47,93,94]

6 Conclusion

We investigated the capabilities of the *PRIMA* instrument *PRIMAger* in detecting AGN, with a particular emphasis on the synergies between *PRIMA* and *NewAthena* in identifying and characterising obscured AGN.

Using X-ray background synthesis models, we predicted the number of AGN as a function of redshift, luminosity, and obscuration, and simulated the fraction of sources detectable by *NewAthena* in Deep (1 deg^2) and Wide (28 deg^2) surveys. For each redshift, luminosity, and obscuration bin, we assigned a set of SEDs from real AGN in the COSMOS field. By convolving the fluxes of these SEDs with the *PRIMAger* instrumental response, we evaluated the detection capabilities of *PRIMA*. Specifically, we simulated two *PRIMA* surveys, each with a 1000-h exposure time and covering the same areas as the *NewAthena* surveys. In addition, we compared our predictions to those achieved with the deepest *Herschel* surveys covering similar regions. Finally, we simulated *PRIMA* measurements of the BHAD evolution, starting with a ~100-μm survey. Our main results are the following:

1. The capabilities of *PRIMA* in measuring the BHAD will surpass those of any current survey. We anticipate achieving precise measurements of the BHAD up to $z \sim 8$, enabling us to determine definitively whether the discrepancy between X-ray-derived estimates and theoretical predictions arises from a population of heavily obscured AGN. Furthermore, *PRIMA* will provide an unprecedented opportunity to study the evolution of AGN and galaxies, probing back to an age of the Universe of ∼700 Myr. Although the BHAD values we obtained depend on the assumed evolution of the total number of AGN, the associated uncertainties do not and effectively illustrate *PRIMA*'s potential in measuring the high-redshift evolution of the BHAD free from obscuration biases. Indeed, we showed that starting from IR-derived BHADs, we can effectively recover the BHAD with even greater accuracy.
2. A Deep *PRIMA* survey will be extremely powerful in revealing AGN up to ∼4 and beyond. We expect to detect ∼30% of all the AGN up to $z \sim 10$ in all the 16 bands and more than 70% in at least one band. On average, we expect to have seven detections per (detected) source. We predict that we will be able to reveal almost the entire AGN population at the "cosmic noon." A Wide survey, on the other hand, will rarely detect AGN $z > 2$. However, thanks to its large area, we expect up to 3×10^5 AGN, of which ∼30,000 with complete detections across all 16 *PRIMAger* bands.
3. The *NewAthena* capabilities in detecting AGN are heavily affected by the source obscuration. With the current survey strategy, most of the CT-AGN (except for the most luminous ones) will be completely missed. For less obscured sources, we will be able to detect most of them up to $z > 2$. Independently from the source obscuration, the most luminous AGN will be visible up to $z \sim 8 - 10$.
4. We found the combination of *PRIMA* and *NewAthena* to be a powerful tool to completely sample the AGN population up to very high-z regardless of the source obscuration. *NewAthena* will be able to detect the most luminous sources and almost all the unobscured AGN, whereas *PRIMA* will be very effective in recovering the heavily obscured and CT-AGN that *NewAthena* will miss. For these sources, it has been shown that SED-fitting or spectroscopic follow-ups with FIRESS will allow us to effectively recognize them as AGN and to characterize their properties.
5. The synergies between the two instruments can also be exploited for the source characterization. A large number of *PRIMA* filters will provide a substantial improvement in our capabilities to perform SED-fitting and properly characterize the host-galaxy and AGN properties at high-z. Moreover, the *NewAthena*-provided X-ray properties can be used to further constrain the SED fitting and overcome the AGN-SF degeneracies. Finally, at high-z even just an X-ray detection should be enough to identify a source as an AGN.
6. Our comparison with the capabilities of existing *Herschel* surveys shows that *PRIMA* will provide an exceptional improvement over existing FIR surveys, both in terms of the numbers of sources and redshift. For the Deep survey, the fraction of detectable AGN at 98 μm increases from ∼10% to ∼60%, with most of them having multiple detections in the other *PRIMAger* bands. The Wide survey perfectly illustrated the capabilities of *PRIMA* in effectively performing large area surveys: we expect an increase in the number of 98 μm-detected sources by a factor ∼30 with respect to *Herschel* surveys covering similar areas.

In this work, we demonstrated the capabilities and the necessity of exploiting the synergies between *PRIMA* and *NewAthena* to detect the full AGN population at and beyond the "cosmic noon" and to effectively characterize these sources. We also highlighted the significant improvement *PRIMA* offers in detecting obscured AGN compared with current surveys and in accurately measuring the evolution of the BHAD. With no planned cryogenically cooled FIR observatories apart from *PRIMA*, we emphasize that without this mission, the astronomical community will face a critical gap in FIR coverage through and beyond 2040. This absence would severely hinder our ability to study obscured AGN and dust-rich galaxies at high redshifts and to finally constrain the evolution of the BH accretion rate density.

Disclosures

The authors have no relevant financial interests in the manuscript or other potential conflicts of interest.

Code and Data Availability

The software POMPA was utilized to estimate the AGN density is available here. The *NewAthena* responses and background can be accessed in the link. The SEDs utilized in this work were obtained from Delvecchio et al. (2015)[95] and can be provided upon request. The latest *PRIMA* capabilities can be found here.

Acknowledgments

LB, LM, and MV acknowledge financial support from the Inter-University Institute for Data Intensive Astronomy (IDIA), a partnership of the University of Cape Town, the University of Pretoria and the University of the Western Cape, and from the South African Department of Science and Innovation's National Research Foundation under the ISARP RADIOMAP Joint Research Scheme (DSI-NRF Grant No. 150551) and the Competitive Programme for Rated Researchers (CPRR) HELP-IDIA Panchromatic PrOject (HIPPO) Project (DSI-NRF Grant No. SRUG22031677). FJC acknowledges funding from grant PID2021-122955OB-C41 funded by MCIN/AEI/10.13039/501100011033 and by ERDF A way of making Europe. Part of the research activities described in this paper was carried out with the contribution of the NextGenerationEU funds within the National Recovery and Resilience Plan (PNRR), Mission 4 - Education and Research, Component 2 - from Research to Business (M4C2), Investment Line 3.1 - Strengthening and creation of Research Infrastructures, and Project IR0000034 - "STILES - Strengthening the Italian Leadership in ELT and SKA." ID acknowledges funding by the European Union - NextGenerationEU, RRF M4C2 1.1, Project No. 2022JZJBHM: "AGN-sCAN: zooming-in on the AGN-galaxy connection since the cosmic noon" - CUP C53D23001120006.

References

1. J. Kormendy and D. Richstone, "Inward bound—the search for supermassive black holes in galactic nuclei," *Annu. Rev. Astron. Astrophys.* **33**, 581 (1995).
2. J. Magorrian et al., "The demography of massive dark objects in galaxy centers," *Astron. J.* **115**, 2285–2305 (1998).
3. L. Ferrarese and D. Merritt, "A fundamental relation between supermassive black holes and their host galaxies," *Astrophys. J.* **539**, L9–L12 (2000).
4. K. Gebhardt et al., "A relationship between nuclear black hole mass and galaxy velocity dispersion," *Astrophys. J.* **539**, L13–L16 (2000).
5. J. Kormendy and L. C. Ho, "Coevolution (or not) of supermassive black holes and host galaxies," *Annu. Rev. Astron. Astrophys.* **51**, 511–653 (2013).
6. P. F. Hopkins et al., "The co-formation of spheroids and quasars traced in their clustering," *Astrophys. J.* **662**, 110–130 (2007).
7. A. Lapi et al., "The coevolution of supermassive black holes and massive galaxies at high redshift," *Astrophys. J.* **782**, 69 (2014).
8. A. Lapi et al., "The dramatic size and kinematic evolution of massive early-type galaxies," *Astrophys. J.* **857**, 22 (2018).
9. J. Silk and M. J. Rees, "Quasars and galaxy formation," *Astron. Astrophys.* **331**, L1–L4 (1998).
10. T. Di Matteo, V. Springel, and L. Hernquist, "Energy input from quasars regulates the growth and activity of black holes and their host galaxies," *Nature* **433**, 604–607 (2005).
11. E. Treister et al., "Major galaxy mergers only trigger the most luminous active galactic nuclei," *Astrophys. J.* **758**, L39 (2012).
12. A. Lamastra et al., "Probing AGN triggering mechanisms through the starburstiness of the host galaxies," *Astron. Astrophys.* **559**, A56 (2013).
13. E. N. Archibald et al., "Coupled spheroid and black hole formation, and the multifrequency detectability of active galactic nuclei and submillimetre sources," *Mon. Not. R. Astron. Soc.* **336**, 353–362 (2002).
14. O. Almaini, "Do sub-mm sources and quasars form an evolutionary sequence?" *Astronomische Nachrichten* **324**, 109–112 (2003).
15. D. M. Alexander et al., "The X-ray spectral properties of SCUBA galaxies," *Astrophys. J.* **632**, 736–750 (2005).
16. P. Madau and M. Dickinson, "Cosmic star-formation history," *Annu. Rev. Astron. Astrophys.* **52**, 415–486 (2014).

17. T. M. Heckman and P. N. Best, "The coevolution of galaxies and supermassive black holes: insights from surveys of the contemporary universe," *Annu. Rev. Astron. Astrophys.* **52**, 589–660 (2014).
18. F. Vito et al., "High-redshift AGN in the Chandra Deep Fields: the obscured fraction and space density of the sub-L_* population," *Mon. Not. R. Astron. Soc.* **473**, 2378–2406 (2018).
19. F. Vito et al., "The hard X-ray luminosity function of high-redshift ($3 < z \lesssim 5$) active galactic nuclei," *Mon. Not. R. Astron. Soc.* **445**, 3557–3574 (2014).
20. J. Aird et al., "The NuSTAR extragalactic survey: first direct measurements of the $\gtrsim$10 KeV X-ray l uminosity function for active galactic nuclei at $z > 0.1$," *Astrophys. J.* **815**, 66 (2015).
21. E. Pouliasis et al., "Active galactic nucleus X-ray luminosity function and absorption function in the Early Universe ($3 \leq z \leq 6$)," *Astron. Astrophys.* **685**, A97 (2024).
22. J. Runburg et al., "Consistent analysis of the AGN LF in X-ray and MIR in the XMM-LSS field," *Astrophys. J.* **924**, 133 (2022).
23. G. Yang et al., "CEERS Key Paper. VI. JWST/MIRI uncovers a large population of obscured AGN at high redshifts," *Astrophys. J.* **950**, L5 (2023).
24. M. Rowan-Robinson et al., "Observations of the Hubble Deep Field with the Infrared Space Observatory - V. Spectral energy distributions, starburst models and star formation history," *Mon. Not. R. Astron. Soc.* **289**, 490–496 (1997).
25. D. H. Hughes et al., "High-redshift star formation in the Hubble Deep Field revealed by a submillimetre-wavelength survey," *Nature* **394**, 241–247 (1998).
26. A. Martnez-Sansigre et al., "The obscuration by dust of most of the growth of supermassive black holes," *Nature* **436**, 666–669 (2005).
27. J. R. Houck et al., "Spectroscopic redshifts to z > 2 for optically obscured sources discovered with the Spitzer Space Telescope," *Astrophys. J.* **622**, L105–L108 (2005).
28. D. Weedman et al., "Active galactic nucleus and starburst classification from spitzer mid-infrared spectra for high-redshift SWIRE sources," *Astrophys. J.* **653**, 101–111 (2006).
29. M. Polletta et al., "Obscuration in extremely luminous quasars," *Astrophys. J.* **675**, 960–984 (2008).
30. S. Mateos et al., "Using the bright ultrahard XMM-Newton survey to define an IR selection of luminous AGN based on WISE colours," *Mon. Not. R. Astron. Soc.* **426**, 3271–3281 (2012).
31. R. J. Assef et al., "Mid-infrared selection of active galactic nuclei with the wide-field infrared survey explorer. II. Properties of WISE-selected active galactic nuclei in the NDWFS Boötes field," *Astrophys. J.* **772**, 26 (2013).
32. I. Delvecchio et al., "Tracing the cosmic growth of supermassive black holes to z 3 with Herschel," *Mon. Not. R. Astron. Soc.* **439**, 2736–2754 (2014).
33. C. Schreiber et al., "The Herschel view of the dominant mode of galaxy growth from z = 4 to the present day," *Astron. Astrophys.* **575**, A74 (2015).
34. C. Gruppioni et al., "The Herschel PEP/HerMES luminosity function - I. Probing the evolution of PACS selected Galaxies to z = 4," *Mon. Not. R. Astron. Soc.* **432**, 23–52 (2013).
35. B. Magnelli et al., "The deepest Herschel-PACS far-infrared survey: number counts and infrared luminosity functions from combined PEP/GOODS-H observations," *Astron. Astrophys.* **553**, A132 (2013).
36. A. Poglitsch et al., "The photodetector array camera and spectrometer (PACS) on the Herschel Space Observatory," *Astron. Astrophys.* **518**, L2 (2010).
37. F. Pozzi et al., "The AGN content in luminous infrared galaxies at z 2 from a global SED analysis including Herschel data," *Mon. Not. R. Astron. Soc.* **423**, 1909–1920 (2012).
38. C. Vignali et al., "The space density of Compton-thick AGN at $z \approx 0.8$ in the zCOSMOS-bright survey," *Astron. Astrophys.* **571**, A34 (2014).
39. P. Tozzi et al., "X-ray spectral properties of active galactic nuclei in the Chandra Deep Field South," *Astron. Astrophys.* **451**, 457–474 (2006).
40. G. Lanzuisi et al., "The Chandra-COSMOS survey - IV. X-ray spectra of the bright sample," *Mon. Not. R. Astron. Soc.* **431**, 978–996 (2013).
41. S. Marchesi et al., "The Chandra COSMOS-legacy survey: source X-ray spectral properties," *Astrophys. J.* **830**, 100 (2016).
42. A. Del Moro et al., "Luminous and obscured quasars and their host galaxies," *Front. Astron. Space Sci.* **4**, 67 (2017).
43. J. Glenn, "PRIMA: the PRobe far-infrared mission for astrophysics," in *Amer. Astron. Soc. Meet. Abstracts, Amer. Astron. Soc. Meet. Abstracts*, Vol. 242, p. 314.02 (2023).
44. C. Bradford et al., "The PRIMA far-infrared probe: observatory and instrumentation," Bulletin of the AAS, Vol. 54 (2022). https://baas.aas.org/pub/2022n6i304p07.
45. A. Moullet et al., "PRIMA general observer science book," arXiv:2310.20572 (2023).
46. M. Béthermin et al., "Confusion of extragalactic sources in the far-infrared: a baseline assessment of the performance of PRIMAger in intensity and polarization," *Astron. Astrophys.* **692**, A52 (2024).

47. L. Bisigello et al., "Disentangling the co-evolution of galaxies and supermassive black holes with PRIMA," *Astron. Astrophys.* **689**, A125 (2024).
48. D. N. Spergel et al., "First-Year Wilkinson microwave anisotropy probe (WMAP) observations: determination of cosmological parameters," *Astrophys. J.* **148**, 175–194 (2003).
49. P. K. Day et al., "A broadband superconducting detector suitable for use in large arrays," *Nature* **425**, 817–821 (2003).
50. J. Baselmans, "Kinetic inductance detectors," *J. Low Temp. Phys.* **167**, 292–304 (2012).
51. P. K. Day et al., "A 25-micron single photon sensitive kinetic inductance detector," arXiv:2404.10246 (2024).
52. J. M. S. Donnellan et al., "Overcoming confusion noise with hyperspectral imaging from PRIMAger," *Mon. Not. R. Astron. Soc.* **532**, 1966–1979 (2024).
53. K. Nandra et al., "The hot and energetic universe: a white paper presenting the science theme motivating the Athena+ mission," arXiv:1306.2307 (2013).
54. D. Barret et al., "The Athena space X'ray observatory and the astrophysics of hot plasma†," *Astronomische Nachrichten* **341**, 224–235 (2020).
55. N. Meidinger et al., "Development status of the wide field imager instrument for Athena," *Proc. SPIE* **11444**, 114440T (2020).
56. L. Barchiesi et al., "The role of SPICA-like missions and the Origins Space Telescope in the quest for heavily obscured AGN and synergies with Athena," *Publ. Astron. Soc. Australia* **38**, e033 (2021).
57. R. Gilli, A. Comastri, and G. Hasinger, "The synthesis of the cosmic X-ray background in the Chandra and XMM-Newton era," *Astron. Astrophys.* **463**, 79–96 (2007).
58. E. Lusso et al., "Bolometric luminosities and Eddington ratios of X-ray selected active galactic nuclei in the XMM-COSMOS survey," *Mon. Not. R. Astron. Soc.* **425**, 623–640 (2012).
59. M. Schmidt, "Space distribution and luminosity functions of quasi-stellar radio sources," *Astrophys. J.* **151**, 393 (1968).
60. W. Saunders et al., "The 60-mu.m and far-infrared luminosity functions of IRAS galaxies.," *Mon. Not. R. Astron. Soc.* **242**, 318–337 (1990).
61. P. F. Hopkins, G. T. Richards, and L. Hernquist, "An observational determination of the bolometric quasar luminosity function," *Astrophys. J.* **654**, 731–753 (2007).
62. I. Delvecchio et al., "SMBH accretion properties of radio-selected AGN out to z4," *Mon. Not. R. Astron. Soc.* **481**, 4971–4983 (2018).
63. W.-H. Bian and Y.-H. Zhao, "Accretion rates and the accretion efficiency in AGNs," *Publ. Astron. Soc. Jpn.* **55**, 599–603 (2003).
64. F. Zhang and Y. Lu, "Extracting the possible intrinsic relation between the radiative efficiency and mass of QSOs: a maximum likelihood method and its application to the SDSS DR7 QSOs," *Astrophys. J.* **902**, 52 (2020).
65. D. Farrah et al., "Stellar and black hole assembly in $z < 0.3$ infrared-luminous mergers: intermittent starbursts versus super-Eddington accretion," *Mon. Not. R. Astron. Soc.* **513**, 4770–4786 (2022).
66. S. J. Oliver et al., "The Herschel multi-tiered extragalactic survey: HerMES," *Mon. Not. R. Astron. Soc.* **424**, 1614–1635 (2012).
67. H. L. Marshall, "The evolution of optically selected quasars with $Z < 2.2$ and $B < 20$," *Astrophys. J.* **299**, 109–121 (1985).
68. Y. Ueda et al., "Toward the standard population synthesis model of the X-ray background: evolution of X-ray luminosity and absorption functions of active galactic nuclei including compton-thick populations," *Astrophys. J.* **786**, 104 (2014).
69. F. Shankar, D. H. Weinberg, and J. Miralda-Escudé, "Accretion-driven evolution of black holes: Eddington ratios, duty cycles and active galaxy fractions," *Mon. Not. R. Astron. Soc.* **428**, 421–446 (2013).
70. D. Sijacki et al., "The Illustris simulation: the evolving population of black holes across cosmic time," *Mon. Not. R. Astron. Soc.* **452**, 575–596 (2015).
71. M. Volonteri et al., "The cosmic evolution of massive black holes in the Horizon-AGN simulation," *Mon. Not. R. Astron. Soc.* **460**, 2979–2996 (2016).
72. P. D. Hurley et al., "HELP: XID+, the probabilistic de-blender for Herschel SPIRE maps," *Mon. Not. R. Astron. Soc.* **464**, 885–896 (2017).
73. L. Wang et al., "Probabilistic and progressive deblended far-infrared and sub-millimetre point source catalogues. I. Methodology and first application in the COSMOS field," *Astron. Astrophys.* **688**, A20 (2024).
74. J. R. Weaver et al., "COSMOS2020: a panchromatic view of the universe to z 10 from two complementary catalogs," *Astrophys. J.s* **258**, 11 (2022).
75. A. Soltan, "Masses of quasars," *Mon. Not. R. Astron. Soc.* **200**, 115–122 (1982).
76. M. Cadoni et al., "Cosmological coupling of nonsingular black holes," *J. Cosmol. Astropart. Phys.* **2023**, 007 (2023).
77. M. Lacy et al., "Constraints on cosmological coupling from the accretion history of supermassive black holes," *Astrophys. J.* **961**, L33 (2024).

78. J. Matthee et al., "Little red dots: an abundant population of faint active galactic nuclei at z5 revealed by the EIGER and FRESCO JWST surveys," *Astrophys. J.* **963**, 129 (2024).
79. I. Labbe et al., "UNCOVER: candidate red active galactic nuclei at $3 < z < 7$ with JWST and ALMA," arXiv:2306.07320 (2023).
80. P. G. Pérez-González et al., "What is the nature of little red dots and what is not, MIRI SMILES edition," *Astrophys. J.* **968**, 4 (2024).
81. C. C. Williams et al., "The galaxies missed by Hubble and ALMA: the contribution of extremely red galaxies to the cosmic census at $3 < z < 8$," *Astrophys. J.* **968**, 34 (2024).
82. H. B. Akins et al., "COSMOS-Web: the over-abundance and physical nature of "little red dots"–implications for early galaxy and SMBH assembly," arXiv:2406.10341 (2024).
83. K. Inayoshi and K. Ichikawa, "Birth of rapidly spinning, overmassive black holes in the early universe," *Astrophys. J.* **973**, L49 (2024).
84. R. Bacon et al., "WST - Widefield Spectroscopic Telescope: motivation, science drivers and top level requirements for a new dedicated facility," *Proc. SPIE* **13094**, 130941O (2024).
85. S. Tommasin et al., "Spitzer IRS high-resolution spectroscopy of the 12 μm Seyfert galaxies. I. First results," *Astrophys. J.* **676**, 836–856 (2008).
86. S. Tommasin et al., "Spitzer-IRS high-resolution spectroscopy of the 12 μm Seyfert galaxies. II. Results for the complete data set," *Astrophys. J.* **709**, 1257–1283 (2010).
87. A. Feltre, S. Charlot, and J. Gutkin, "Nuclear activity versus star formation: emission-line diagnostics at ultraviolet and optical wavelengths," *Mon. Not. R. Astron. Soc.* **456**, 3354–3374 (2016).
88. Y. Wu et al., "Spitzer/IRS $5 - 35$ μm low-resolution spectroscopy of the 12 μm Seyfert sample," *Astrophys. J.* **701**, 658–676 (2009).
89. Y. Shi et al., "9.7 μm silicate features in active galactic nuclei: new insights into unification models," *Astrophys. J.* **653**, 127–136 (2006).
90. A. D. Goulding et al., "Deep silicate absorption features in compton-thick active galactic nuclei predominantly arise due to dust in the host galaxy," *Astrophys. J.* **755**, 5 (2012).
91. C. Gruppioni et al., "Tracing black hole accretion with SED decomposition and IR lines: from local galaxies to the high-z Universe," *Mon. Not. R. Astron. Soc.* **458**, 4297–4320 (2016).
92. A. Leger, L. D'Hendecourt, and D. Defourneau, "Physics of IR emission by interstellar PAH molecules," *Astron. Astrophys.* **216**, 148–164 (1989).
93. M. Meixner et al., "Origins space telescope mission concept study report," arXiv:1912.06213 (2019).
94. S. Mordini, L. Spinoglio, and J. A. Fernández-Ontiveros, "Calibration of mid- to far-infrared spectral lines in galaxies," arXiv:2105.04584 (2021).
95. I. Delvecchio et al., "Mapping the average AGN accretion rate in the SFR-M* plane for Herschel-selected galaxies at $0 < z \leq 2.5$," *Mon. Not. R. Astron. Soc.* **449**, 373–389 (2015).

Biographies of the authors are not available.